Optical constants and thickness determination of La 2 / 3 Sr 1 / 3 MnO3 thin films on Nb:SrTiO3 substrates by spectro-ellipsometry: Combination of optical and X-ray techniques

Jérémy Blond, Christian Dufour, Sandeep Kumar Chaluvadi, Sylvain Duprey, Xavier Portier, Philippe Marie, Victor Pierron, Laurence Méchin, Bruno Guillet

=0pt

Graphical Abstract

Optical constants and thickness determination of $La_{2/3}Sr_{1/3}MnO_3$ thin films on $Nb:SrTiO_3$ substrates by spectro-ellipsometry: combination of optical and X-ray techniques

Jérémy Blond,Christian Dufour,Sandeep Kumar Chaluvadi,Sylvain Duprey,Xavier Portier,Philippe Marie,Victor Pierron,Laurence Méchin,Bruno Guillet

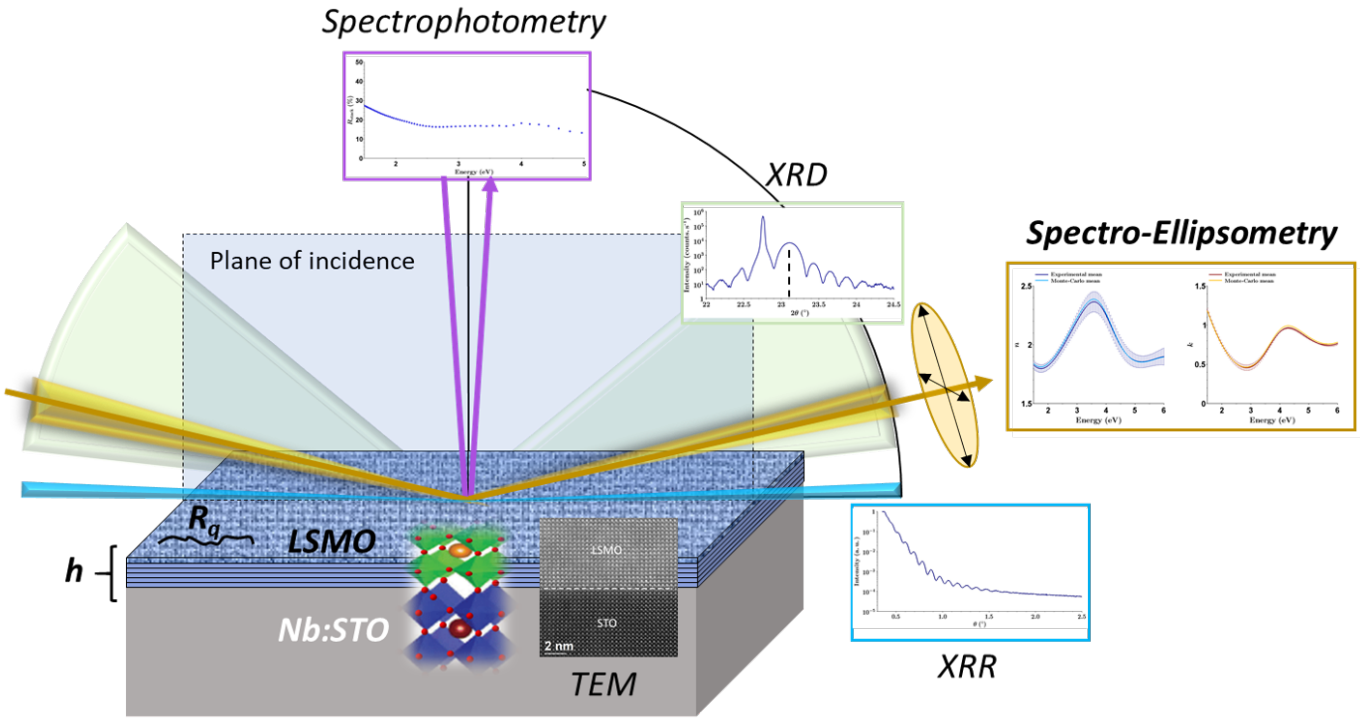

Highlights

Optical constants and thickness determination of $La_{2/3}Sr_{1/3}MnO_3$ thin films on Nb:$SrTiO_3$ substrates by spectro-ellipsometry: combination of optical and X-ray techniques

Jérémy Blond,Christian Dufour,Sandeep Kumar Chaluvadi,Sylvain Duprey,Xavier Portier,Philippe Marie,Victor Pierron,Laurence Méchin,Bruno Guillet

- Physically-based accurate ellipsometric modelling of heteroepitaxial manganite
- Simultaneous estimation of LSMO thickness, roughness, mass density and optical gap
- Quantitative matching between X-ray and optical techniques on thin film

Optical constants and thickness determination of $La_{2/3}Sr_{1/3}MnO_3$ thin films on Nb:$SrTiO_3$ substrates by spectro-ellipsometry: combination of optical and X-ray techniques

Jérémy Blond[a,*], Christian Dufour[b], Sandeep Kumar Chaluvadi[c], Sylvain Duprey[b], Xavier Portier[b], Philippe Marie[b], Victor Pierron[a], Laurence Méchin[a] and Bruno Guillet[a]

[a]Normandie Univ, UNICAEN, ENSICAEN, CNRS, GREYC, 14000 Caen, France
[b]Normandie Univ, ENSICAEN, UNICAEN, CEA, CNRS, CIMAP, 14000 Caen, France
[c]CNR-IOM – Istituto Officina dei Materiali, Consiglio Nazionale delle Ricerche, Trieste, 34149, Italy

ARTICLE INFO

Keywords:
Oxide heterostructure
Spectro-ellipsometry
Spectrophotometry
X-ray characterization
Cross-analysis

ABSTRACT

40 nm thick $La_{2/3}Sr_{1/3}MnO_3$ (LSMO) thin films were epitaxially grown by Pulsed Laser Deposition (PLD) onto niobium doped $SrTiO_3$ (Nb:STO) substrates, with different Nb concentration from 0.01 %wt to 0.5 %wt. The optical characterization of the heterostructures by spectroscopic ellipsometry enables us to extract the optical constants of the manganite heteroepitaxial layer at room temperature. Performing spectrophotometry in the same wavelength range brings a useful cross-validation of the extracted results. In addition, the thickness evaluation of the LSMO layer by spectro-ellipsometry is further validated by both High Resolution X-ray diffraction and X-ray reflectivity, as well as a Transmission Electron Microscopy cross section, taken as a physical reference. This study validates quantitatively the spectro-ellipsometry as a suitable routine tool to measure accurately both thickness and complex refractive index of the LSMO thin film, picturing their peculiar electrical behaviour between both metallic and insulating phases. The relative error on the thickness measurement between X-ray and ellipsometry is less than 5 %. The LSMO complex refractive index enabled also a simultaneous estimation of further material properties, such as the optical gap ω_g or the mass density ρ_m, determined with less than 1.5 % relative error compared to X-ray reflectivity results.

1. Introduction

Perovskite oxide heterostructures are attracting a lot of interest due to their distinguishing properties that could emerge from the combination of strong correlated electron systems, like good rectification characteristics [1–5] or giant photoresponse [6]. Among them, the lanthanum strontium manganite on niobium-doped strontium titanate is often reported as a promising candidate for photodetection [7, 8]. Using the composition $La_{2/3}Sr_{1/3}MnO_3$ for LSMO, which is a metallic phase at room temperature, the electrical behaviour of the heterostructure is comparable to a Schottky diode one. LSMO plays the anode role and the semiconducting Nb:$SrTiO_3$ the cathode one. This opens the way of two modes of photodetection, either internal photoemission process over the Schottky barrier or bandgap absorption in the Nb:STO. In order to properly design such a Schottky barrier photodetector, knowing the optical characteristics of each layer is of importance. Such an extended optical characterization of the LSMO and Nb:STO from UV to near-infrared radiation is sparsely represented in the literature. That is the reason why this paper is focusing on the validation of the spectroscopic ellipsometry modelling of the LSMO layer. The resulted dispersion model is compared with a specular reflective measurement on the same wavelength range, i.e. 1.5 – 5.0 eV, while the thickness estimation of the LSMO is cross checked with X-ray Reflectivity (XRR) and Transmission Electron Microscopy (TEM). The related optical conductivity at room temperature is also compared with that from DC electrical resistivity measurement. As previously done by Yamada *et al.* on MgO substrate [9], the free-carrier concentration is discussed. An estimation of the mass density of $La_{2/3}Sr_{1/3}MnO_3$ on Nb:STO substrates is also presented, derived from both ellipsometry and X-ray reflectivity.

*Corresponding author
jeremy.blond@unicaen.fr (J. Blond)
ORCID(s): 0000-0001-7257-5338 (J. Blond)

2. Material and methods

2.1. Heterostructure fabrication

A thin layer of $La_{2/3}Sr_{1/3}MnO_3$ is deposited by pulsed laser deposition (PLD), from a solid target of the same composition, on (001) oriented niobium doped $SrTiO_3$ (Nb:STO) substrate, from Crystec GmbH. During growth, the sample is maintained at 730 °C, under a partial oxygen pressure of 0.2 mbar. The PLD process is using a 248 nm KrF laser, pulsed at 3 Hz, with a fluence of 1.7 J.cm^{-2}. After growth completion, the sample is then cooled down to room temperature at 10 °C.min^{-1} rate, with an oxygen pressure of 500 mbar. This latter part of the process is made for ensuring the nominal stoechiometry of oxygen in the LSMO layer. Five samples of 10×5 mm^2, with different Nb concentrations from 0 to 0.5 %wt, have been processed.

2.2. Heterostructure characterization

The optical properties as well as the thickness of the LSMO layer have been studied from ultraviolet to near-infrared wavelengths by spectroscopic ellipsometry. The

measurement has been performed using an UVISEL ellipsometer from Horiba Jobin-Yvon, in an energy range from 1.5 up to 6 eV with a 0.05 eV step and an incidence angle of 70°. The comparison with other characterization techniques has been useful to confirm the relevancy of the ellipsometric model of the top layer. Some interesting properties of the LSMO thin film at room temperature could then be estimated with more confidence, such as its mass density or its optical gap.

2.2.1. Spectro-ellipsometry

An usual ellipsometer is often a tabletop tool with only an affordable low-power Xenon arc lamp as a light source, associated with a monochromator. Therefore, it represents a good compromise between sensitivity, speed and ease to handle. However, an ellipsometric measurement is only indirect and requires the correct modelling of the stack to find out some reliable value on the desired material properties. In fact, the phase modulated ellipsometer are measuring light intensities that enable the determination of the ellipsometric angles Δ and Ψ, as defined in [10]. The complex ratio ρ defined by relation (13) in Appendix A.1 depends of the incident photon energy E [9]. With Fresnel equations at interfaces and a transfer-matrix method, ellipsometric quantities can be calculated from an appropriate analytical dispersion model of each layer in the measured material stack, i.e. their optical indexes [11]. Therefore, a dedicated numerical procedure implements a non-linear least-square fit to find the best corresponding parameter values to minimize the chi squared χ^2_{SE} figure of merit between the measured intensities I_c and I_s by the ellipsometer, which equals $2\cos(2\Psi)\cos\Delta$ and $2\cos(2\Psi)\sin\Delta$ respectively. The χ^2_{SE} represents the sum of the squared errors between experimental each data points $\left(I_c(E), I_s(E)\right)$ and the simulated ones from the spectro-ellipsometric model [12]. Obtaining a χ^2_{SE} value inferior to 1 on complex dispersion model, such as the LSMO one, is considered as a very good fit [13].

An appropriate model for the LSMO/Nb:STO stack was built using the software Deltapsi2 [14], including a semi-infinite substrate, the Nb:STO, topped by an homogeneous thin layer of LSMO. The fitting of experimental data, i.e. ellipsometric angles Ψ and Δ, provides the thickness determination of the thin layer h and its complex refractive index $\hat{n}$, i.e. its refractive index n and its extinction coefficient k.

The modelling of the ferromagnetic LSMO is physically based on a mix of a Drude dispersion model, to take into account its metallic phase, associated with a double-oscillator dielectric model for the semiconducting behaviour. The chosen oscillator formulation is a derivation of the Forouhi-Bloomer model, that can be used to describe the frequency dependence of the complex refractive index of a semiconductor near or above its optical gap. In total, the whole ellipsometric model contains eleven parameters to fit the experimental data, including the layer thickness.

2.2.2. X-ray characterization

First, to confirm independently the thickness value found by ellipsometry, some X-ray measurements have also been performed on the samples with a Malvern Panalytical Empyrean diffractometer, in the diffraction mode (XRD) with a θ-2θ configuration, from 20° up to 80°, and also in the reflectivity mode at grazing angles (XRR). For the high resolution X-ray diffraction (HRXRD), a monochromated X-ray wavelength Cu $K_{\alpha 1}$ (1.5406 Å) is used. The diffraction spectra analysis of such single crystalline film allows the determination of its cystallographic structural properties as well as its thickness. In the XRR case, the X-ray radiation beam from the Cu anode is composed on equal part by Cu $K_{\alpha 1}$ (1.5406 Å) and Cu $K_{\alpha 2}$ (1.5444 Å) wavelengths. The angle between the incident beam and the detector is 2θ, ranging from 0.7° and 5°. The resulting spectra were analyzed using two different methods. The first one is related to an inverse Fourier transform, that gives access to the position in depth of each interface in the measured stack. The second consists in the fitting of the spectra by the dedicated GenX software [15].

2.2.3. TEM cross-section

The accuracy of the indirect thickness measurement of the LSMO layer is also investigated by Transmission Electron Microscopy (TEM). Cross-section allowing the electron beam to be parallel to the film/substrate interface has been prepared by Focused Ion Bean (FIB) owing to a Dual beam FEI Helios nanolab 660. Prior to the thinning process, a sputtered 10 nm thick carbon film and a few micron thick platinum layer have been deposited at the top of the film. The carbon film purpose is to discriminate the top of the film from Pt which protect the whole structure from the Ga beam milling process. The microscope used is a Cold FEG double corrected JEOL ARM200 microscope, operated at 200 kV and equipped with a High Angle Annular Dark Field detector (HAADF) as well as a scanning setup. The point to point resolution value is 0.78 Å.

2.2.4. Spectrophotometry

Then, in order to validate this dispersion model, the optical reflectance of the heterostructure for an unpolarized light is calculated thanks to the Fresnel formalism and a transfer matrix method, equivalent to (14) with (8), using the complex refractive indexes $\hat{n}$ of each material, provided by the spectro-ellipsometer. This simulated reflectance is then compared with the one directly measured by a Perkin Elmer 1050 Lambda UV-Vis-NIR dual-beam spectrophotometer equipped with an Universal Reflectance Accessory (URA) at 8° incidence angle.

2.2.5. Electrical measurement

The free carrier concentration inside the LSMO layer can be also roughly estimated thanks to the data coming from an in-line four-point probe DC resistivity measurement with a bias current I of 60 µA. Given the interprobe spacing of 2 mm and the rectangular sample size of 10 × 5 mm^2, a geometrical correction factor C_{geom} has to be applied to

calculate the sheet resistance, instead of the well-known coefficient $\pi/ln(2)$ for an infinite slice, according to [16]. Taking into account the small difference between the value provided by Smits and the more recent one from Perloff [17], a mean calculated value of $C_{geom} = 2.37$ has been chosen. The related sheet resistance R_s, expressed in $\Omega.\square^{-1}$, is then computed by the following equation [16].

$$R_s = \frac{\rho_{dc}}{h_{\mathrm{LSMO}}} = C_{geom}\frac{V}{I} \quad (1)$$

Where ρ_{dc} represents the static electrical resistivity and h_{LSMO} the LSMO layer thickness.

2.3. Numerical methods

Given the HRXRD experimental angular increment of 0.01°, a Savitzky-Golay third-degree polynomial filtering has been done to smooth the raw data. The purpose of this data treatment is to remove any high-frequency fringe peak artifact detection during the automatic peak search numerical procedure, using the zero-crossing of the first derivative of the HRXRD signal intensity.

In order to take into account the related error, introduced by the extraction procedure, each peak maximum position has been randomly sampled independently 5000 times in a Monte-Carlo way, by adding, ignoring or removing a step value of 0.02°, corresponding to twice the instrumental angular scan resolution. Consequently, the related standard deviation, calculated from all the drawn results resulting from equation (4), is used to estimate the thickness of the LSMO layer with a 2-σ dispersion interval.

A similar numerical treatment is applied on XRR spectra in order to determine automatically the Kiessig fringe position. The uncertainty evaluation methodology is also the same as for HRXRD case, i.e. by randomizing here a peak positional error, equals to twice the XRR experimental angular increment of 0.008° with a Monte-Carlo procedure, considering a uniform statistical law. It gives a maximum uncertainty less than two LSMO atomic planes, around 0.6 nm. The main advantage of this method is to reduce the relative uncertainty on the thickness determination compared to the Fourier transform analysis, also performed in our study and limited by a lower intrinsic resolution. However, the drawback of this peak detection method is to not quantify the LSMO layer roughness, like the Fourier analysis can do.

A Monte-Carlo method is also implemented to estimate the mean value for the refractive index n and the extinction coefficient k of the LSMO layer, considering a gaussian dispersion law on each of the 10 parameters of the spectro-ellipsometric dispersion model. This numerical procedure of 10000 random sampling is used here to consolidate the confidence in the n and k values given by the analysis made by the ellipsometer DeltaPsi2 software [13].

Each 2-σ uncertainty, presented in the tables of this work, are due to either instrumental resolution, fitting procedure or numerical treatment. σ_i designates the related standard deviation for the considered physical quantity for the i^{th} sample.

Considering now the 2-σ confidence interval on the mean values, the calculation of the standard deviation σ_{mean} is based on the following formula:

$$\sigma_{mean} = \sqrt{\sigma^2_{sample} + < \sigma_i >^2} \quad (2)$$

Where σ_{sample} designates the standard deviation between the measured samples.

3. Results and discussion

Five LSMO/Nb:STO heterostructures were prepared and analyzed, corresponding to five different Nb content, i.e. 0 %wt (pure STO), 0.01 %wt, 0.05 %wt, 0.1 %wt, 0.5 %wt. For each one, the LSMO thin film has been deposited within the same PLD conditions, showing an expected $La_{2/3}Sr_{1/3}MnO_3$ theoretical composition, with a nominal thickness of 40 nm. The main difference between the samples is the niobium concentration of the Nb:STO of the substrate. The Nb atoms, with a 5+ ionization state in a substitutional position in the lattice perovskite, acts as a donor of electrons by replacing the Ti^{4+} ions. The more the Nb content is important, the more the electrical conductivity increases. In the visible range, the apparent color changes from transparent for $SrTiO_3$ to very dark for 0.5 %wt, revealing already a progressive absorption in the studied wavelength range. First, some structural properties of the heterostructure are deduced from X-ray diffraction (XRD) spectra analysis.

3.1. X-ray characterization of the heterostructure

3.1.1. X-ray diffraction analysis

It is important to check the crystalline growth of the LSMO layer onto Nb:STO substrates, whatever the Nb concentration considered here. Figure 1 (a) shows the XRD pattern in the θ-2θ configuration from 20° up to 80°. It is clearly visible that only the first 3 orders of diffraction for (00l) orientation are present, indicating an heteroepitaxial growth of the LSMO film onto all the substrates, whatever the considered Nb concentration. In addition, Figure 1 (b) diplays a high resolution XRD spectrum example for the (001) line for the LSMO/STO heterostructure. The so-called *Pendellösung* fringes or *Laue* oscillations, typical of a coherent X-ray scattering of the (001) diffracting planes within the thin film, are well-defined up to the 4th-order fringe. This particular feature indicates a high crystallinity of the LSMO film [18, 19]. As it is already extensively described in the literature, a straightforward analysis of such XRD spectrum enables to extract several structural properties on the heterostructure under study. First, the lattice parameter in the perpendicular z direction for both the substrate and the film can be inferred using the common Bragg law [20]. In our case, it corresponds to the cross-plane lattice parameter of either the substrate $c_{Nb:STO}$ or the layer c_{LSMO} depending of the chosen Bragg angle diffraction θ_B. The second parameter is related to the thickness of the film, which could be calculated using the angular period of the fringes maxima [18, 21]. Here, we do not consider any mismatch angle between

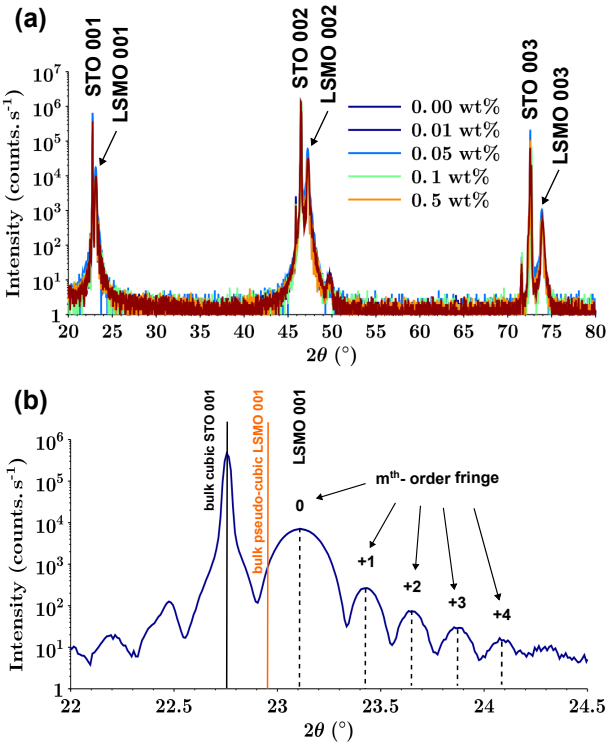

Figure 1: X-ray diffraction pattern in the θ-2θ configuration of LSMO films deposited (a) on Nb:STO substrates with different Nb doping concentration, for the 20° - 80° 2θ range and (b) on STO substrate, with a high resolution profile around the (001) line, i.e. for the 22° - 24.5° 2θ range.

the substrate surface and the film planes, i.e. the LSMO layer has grown perfectly coplanar to the substrate. Therefore, the following expression is applicable [22].

$$\Delta\theta_m = \frac{\lambda}{2h\cos(\theta_m)} \tag{3}$$

Here, $\Delta\theta_m$ designates the distance between two fringe maxima and h the thickness of the LSMO layer. The scattering vector norm is defined by $q_z = (4\pi/\lambda)\sin(\theta)$ [20]. Combining equation (3) and the first derivative of q_z with respect to θ gives the relationship $\Delta q_{z-m} = 2\pi/h$ [23].

Therefore, in the q-scale, the differential of the fringe scattering vector is constant. Here, the order numbering of the fringe is the implicit differenciation variable, given that $\Delta m = 1$. The thickness h of the epilayer is directly related to the slope of the fringe order versus the fringe maxima position in the q-scale:

$$h = 2\pi\frac{\Delta m}{\Delta q_{z-m}} \tag{4}$$

The third quantity that can be extracted of such XRD profile concerns the strain of the epifilm. In Figure 1 (b), the position of the bulk pseudo-cubic (001) diffraction line for the LSMO has been added for clarity. As the cubic lattice parameter of the STO or Nb:STO substrate ($c_{Nb:STO} = c_{STO} = 3.905$ Å) is larger than the LSMO bulk pseudo-cubic one ($c_{LSMOpc} = 3.873$ Å) [24], the later material is experiencing an in-plane tensile strain during the epitaxial growth and, naturally, an out-of-plane compressive strain. For films with thickness under 60 nm, the LSMO remains fully strained because the out-of-plane lattice parameter c_{LSMO} is almost constant from the interface with the substrate up to the top of the film [25]. The cross-plane lattice deformation $\epsilon_{[001]}$ of the LSMO layer is defined using the relative deviation ratio between its the bulk pseudo-cubic lattice parameter and the measured one [26]. It represents a quantitative evaluation of the out-of-plane compression degree of the LSMO layer.

The results, compiled in Table (1) and Table (2), have been extracted from HRXRD spectra, around the (001) line and around the (002) line respectively. The values of LSMO thickness are consistent for each heterostructures between the two diffraction lines. The $\epsilon_{[001]}$ values are fairly close to the already published value of -0.57 % for a 40-nm-thick LSMO layer grown by PLD over an (001) STO substrate [26]. As expected for Nb:STO substrates, all the epitaxial LSMO layers seem very similar one to each other, considering the extracted parameters from HRXRD analysis.

Their excellent cristallinity is also illustrated by the TEM observations of sample n° 1 reported in Figure 2. A typical cross sectional low magnification bright field image of the entire structure (STO/LSMO/C/Pt) along the [100] direction of both STO and LSMO materials is presented in Figure 2 (a). A thickness variation of the LSMO film between 40 nm and 43 nm is observable. Figure 2 (b) is an enlarged view (STEM HAADF) of the STO/LSMO interface at the atomic scale. The chemical Z-constrast reveals a perfect fit of the atomic arrangement at the interface due to the small lattice mismatch, inferior to 1 %, between the two cubic structures of STO and LSMO (see previous paragraph). The brighter constrast observed for LSMO is explained by its higher average atomic number Z (19.9) compared to that of STO (16.8). The inset at the top right-hand side is enlarging the interfacial region. The inset at the bottom right-hand side is a Fast Fourier Transform (FFT) of the entire image, confirming the cubic projection along the [100] directions of both materials with the (001) planes parallel to the interface. The LSMO film is thus reproducing perfectly the crystalline orientation of the substrate. No misfit dislocation has been observed in the investigated sample region.

3.1.2. X-ray reflectivity measurement

A material response to an incident illumination involves different relaxation mechanisms that depend of the wavelength. They are described by the material complex dielectric function or alternatively by its complex refractive index. For X-rays, the linear refractive index of a material equals $\hat{n} = 1 - \delta - j\beta$, with coefficients δ and β representing respectively scattering and absorption effects, specific to each material [27]. δ is in the order of 10^{-5} - 10^{-6}, which is low compared to 1. As $|\beta|$ is one order of magnitude lower than $|\delta|$ in general, we are neglecting here the absorption effect, which is commonly done elsewhere [28]. The mathematical formalism to quantify the specular light reflectance from the sample top surface in X-ray, $R\left(q_z\right)$, is similar to the

Table 1
Properties of the LSMO layer, extracted from (001)-line HRXRD profile analysis: out-of-plane lattice parameter c_{LSMO}, out-of-plane compression degree $\epsilon_{[001]}$ and layer thickness h_{LSMO}, with 2-σ uncertainty obtained from Monte-Carlo method. The 2-σ uncertainty on the mean values includes in addition the sample dispersion (see details in Numerical methods of section 2).

N°	[Nb] (%wt)	c_{LSMO} (Å)	$\epsilon_{[001]}$ (%)	h_{LSMO} (nm)
1	0	3.846 ± 0.005	- 0.73 ± 0.14	37.6 ± 1.6
2	0.01	3.843 ± 0.005	- 0.73 ± 0.14	40.1 ± 1.9
3	0.05	3.846 ± 0.005	- 0.69 ± 0.14	38.9 ± 1.7
4	0.1	3.843 ± 0.005	- 0.73 ± 0.14	40.9 ± 2.0
5	0.5	3.843 ± 0.005	- 0.81 ± 0.14	40.9 ± 1.9
Mean		**3.844 ± 0.006**	**- 0.74 ± 0.17**	**39.7 ± 3.4**

Table 2
Properties of the LSMO layer, extracted from (002)-line HRXRD profile analysis: out-of-plane lattice parameter c_{LSMO}, out-of-plane compression degree $\epsilon_{[001]}$ and layer thickness h_{LSMO}, with 2-σ uncertainty obtained from Monte-Carlo method. The 2-σ uncertainty on the mean values includes in addition the sample dispersion (see details in Numerical methods of section 2).

N°	[Nb] (%wt)	c_{LSMO} (Å)	$\epsilon_{[001]}$ (%)	h_{LSMO} (nm)
1	0	3.845 ± 0.003	- 0.73 ± 0.07	34.9 ± 1.9
2	0.01	3.846 ± 0.003	- 0.71 ± 0.06	39.4 ± 1.7
3	0.05	3.842 ± 0.003	- 0.79 ± 0.07	38.6 ± 1.6
4	0.1	3.845 ± 0.003	- 0.73 ± 0.06	39.8 ± 1.7
5	0.5	3.842 ± 0.003	- 0.81 ± 0.06	40.6 ± 1.8
Mean		**3.844 ± 0.004**	**- 0.76 ± 0.11**	**38.7 ± 4.7**

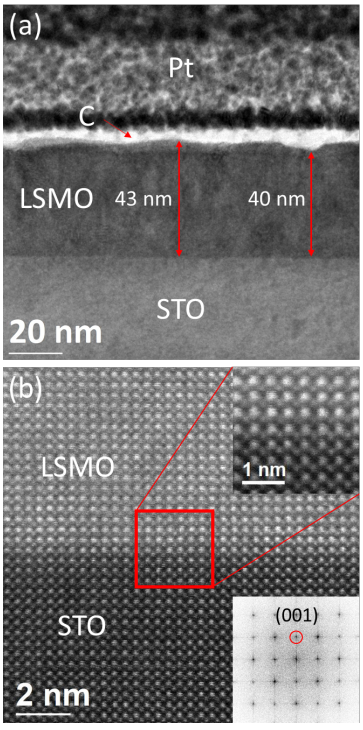

Figure 2: TEM cross-section observation of sample 1 following the [001] direction of STO (a) Low magnification bright field image, with LSMO thickness estimation (b) high resolution image, focused on the LSMO/STO interface.

one used in optical reflectometry, i.e. Snell-Descartes and Fresnel equations applied to a single-layer heterostructure [18, 27]. Here, q_z designates the scattering vector corrected for refraction inside the thin film [29]:

$$q_z = 4\pi \frac{\sqrt{\cos^2\theta_c - \cos^2\theta}}{\lambda} \tag{5}$$

where θ is the grazing incidence angle, θ_c is the critical angle for total reflection and λ is the considered X-ray wavelength. In the case of null absorption and within the frame of Born approximations, the kinematical theory relates the X-ray reflection to the Auto Correlation Function (ACF) of the first derivative of the electron density versus depth $\rho'(z)$ [27]. Unlike the dynamical theory that requires numerical modelling and non-linear fitting procedures, the determination of the interfaces location in depth is model-free by computing the reverse Fourier transform of the measured reflectivity, normalized by the Fresnel reflectivity of the substrate. The ACF of $\rho'(z)$ can be then calculated using the following relation, provided q_z values are equally spaced.

$$\rho'(z) * \rho'(z) = TF^{-1}\left[\rho_s^2 \frac{R(q_z)}{R_F(q_z)}\right] = TF^{-1}\left[\frac{q_z^4 R(q_z)}{(4\pi r_e)^2}\right] \tag{6}$$

where R_F is the Fresnel reflectance of the substrate, ρ_s the electron density inside the substrate and r_e is the classical electron radius.

Concerning the X-ray reflectance model of a single layer heterostructure, the expected curve should exhibit some peculiar interference patterns, called Kiessing fringes, as shown in Figure 3 (a). The maxima of these oscillations are observed when constructive interference condition is respected. This is equivalent to a Bragg condition corrected for refraction with $h(q_z/2\pi) = m$ where h is the layer thickness and m an integer.

Analysing the peak positions in the $|ACF(\rho'(z))|$ curve gives directly access to the layer thicknesses in a stack, which was already well-pictured by Bridou *et al.* [29]. Figure 3 (b) displays the ACF of the electron density depth gradient for sample n° 1, i.e. the LSMO/STO heterostructure without Nb doping. The second peak, namely 3-1 in the inset window of the figure, indicates the position of the interface LSMO/STO, situated around 40 nm in depth from the top interface air/LSMO, located at z = 0. However, the main drawback of this technique could be the depth resolution $\Delta z = 2\pi/(q_{z-max} - q_{z-min})$, directly related to the scattering window, i.e. the angular window of the measurement.

Therefore, to obtain a high resolution Fourier analysis on an XRR measurement, one has to consider a sufficient grazing angle range. In our case, as shown in Figure 3 (a), the highest measured angle is $\theta = 2.5°$, i.e. $\Delta z \approx 1.9$ nm. This minimum step uncertainty represents about 5 atomic planes for the

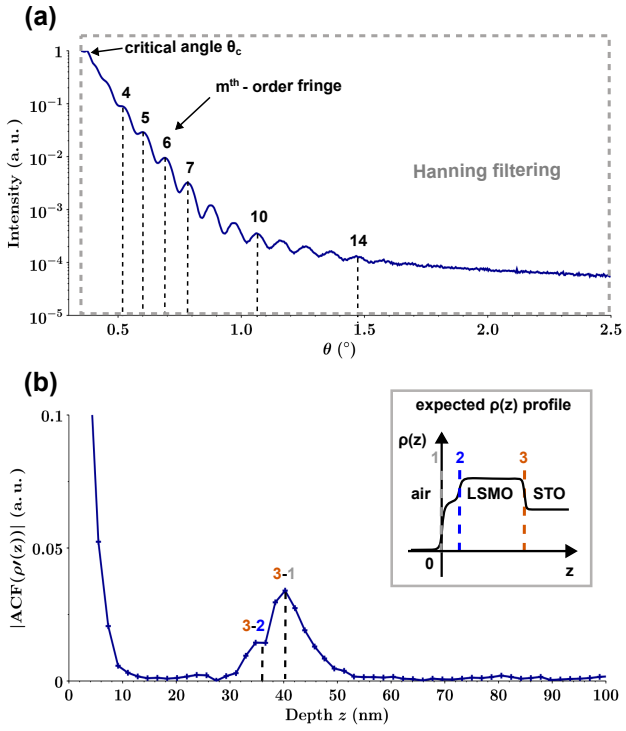

Figure 3: X-ray reflectivity analysis of the LSMO/STO heterostructure (sample n°1) (a) XRR intensity curve versus θ. (b) Autocorrelation function of $\rho'(z)$ inside the heterostructure (inset with the expected $\rho(z)$ shape from ACF peak analysis).

LSMO under study and around 5 % of a 40-nm thick layer, which could lead to a non-negligible bias error in the LSMO thickness determination. For instance, in order to keep this step uncertainty around 1 %, the maximum measured angle should have been 10°. Nevertheless, this experimental step uncertainty is not higher than the one outlined in Table 2 for XRD measurement. The Fourier analysis method is in any case suitable to consolidate the confidence in the LSMO thickness value, as demonstrated in Figure 3 (b) for sample n° 1.

The absolute value of the ACF of the electron density gradient spectrum exhibits two convoluted peaks, due to the low above-mentioned XRR angular resolution. The higher peak, namely 3-1 in the inset window of Figure 3 (b), corresponds directly to the entire LSMO layer thickness, as expected for a single layer heterostructure. The significant peak broadening, with an half-width at half maximum around 3.6 nm in this case, could be due to a soft electron density gradient at interfaces [27].

On the other hand, the smaller peak, namely 3-2 in the inset window of Figure 3 (b), corresponds to the LSMO thickness whose the electronic density is constant versus depth. This latter region could be rough, as indicated by the quick damping of the XRR intensity when the incidence angle is increasing (see Figure 3 (a)). This is confirmed by the TEM cross-section of Figure 2 (a), where a thickness variation of the LSMO layer about 3 nm is clearly observable. An estimation of the rms roughness could be made by substracting the z positions of the two visible peaks of Figure 3 (b) and divided the result by 2. Given the low experimental resolution, this roughness estimation $\hat{R}_q$, reported in Table 3, represents only an approximation, with a missing 2-1 peak around 4 nm that cannot be resolved here. Nevertheless, this interpeak interval is in fair agreement with the previous published rms roughness value of 2.2 nm for a PLD grown LSMO thin film [30].

The LSMO thickness evaluation from XRR spectra, i.e. the entire layer including the roughness region, is summarized in table 3 for the 5 measured samples. In this case, the uncertainty on the thickness evaluation is taken directly equal to Δz, i.e. the experimental angular resolution of the XRR spectra. In addition of the Fourier analysis, it is also possible to implement a linear regression analysis including the squared angular position of the fringe peak maxima θ_{max} and their squared ordering. The next formula is easily obtained [23].

$$\theta_{max}^2 = \theta_c^2 + m^2 \left(\frac{\lambda}{2h}\right)^2 \tag{7}$$

The layer thickness is then calculated with the slope of θ_{max}^2 with respect to m^2, extracted from the linear fit of experimental data, based on (7) [23]. This data treatment provides a maximum uncertainty less than two LSMO atomic planes, around 0.6 nm, but does not give information about the roughness of the thin film as the Fourier analysis does. The results of both methods, including the previous described errors, are summarized in Table 3. Compared to XRD sensitive to perfect cristalline diffracting planes inside the LSMO layer, XRR measurement is sensitive to electron density contrast, i.e. the interface constrast air/LSMO and LSMO/Nb:STO. As expected, the thickness values extracted from the XRR analysis are between 1 to 4 nm higher than those calculated from HRXRD data, which seems to be related to the top surface roughness, as suggested by the TEM picture presented in Figure 2 (a). The thickness extracted from HRXRD analysis could be then see as a minimum threshold thickness for the LSMO epitaxial film.

The critical angle for total external reflection θ_c could be determined directly from the XRR curves, without using (7). θ_c corresponds to the first angle where the XRR intensity starts to decrease, after a plateau at the maximum intensity value, provided that the X-ray beam footprint is within the sample area, according to Gibaud *et al.* [27]. Its value is a picture of the mass density ρ_m of the top LSMO layer of the heterostructure, thanks to some calculations detailed in Appendix A.2. The values for each sample are reported in Table 3.

3.2. Optical characterization of LSMO by spectro-ellipsometry

The X-ray techniques constitute suitable reference tools for the non-destructive characterization of materials, especially to determine the cristallographic structure, the thickness as well as the density of thin films, even with nanometric layer because of the ultra-short wavelengths. However,

Table 3
LSMO layer properties determined by X-ray reflectivity: thickness from peak analysis $h_{LSMO\text{-}XRR\ peaks}$, thickness from Fourier transform $h_{LSMO\text{-}XRR\ Fourier}$, roughness estimation $\hat{R}_q$, critical reflection angle θ_c, mass density ρ_m. The 2-σ uncertainties are derived directly from the instrumental angular resolution, except for $h_{LSMO\text{-}XRR\ peaks}$ with errors calculated from a Monte-Carlo approach. The 2-σ uncertainty on the mean values includes in addition the sample dispersion.

N°	[Nb] (%wt)	$h_{LSMO\text{-}XRR\ peaks}$ (nm)	$h_{LSMO\text{-}XRR\ Fourier}$ (nm)	$\hat{R}_q$ (nm)	θ_c (°)	ρ_m ($g.cm^{-3}$)
1	0	41.0 ± 0.3	40.3 ± 1.9	2.2 ± 0.9	0.38 ± 0.02	7.18 ± 0.61
2	0.01	45.0 ± 0.3	44.0 ± 1.9	2.8 ± 0.9	0.40 ± 0.02	7.96 ± 0.64
3	0.05	41.2 ± 0.6	42.2 ± 1.9	2.8 ± 0.9	0.40 ± 0.02	7.96 ± 0.64
4	0.1	43.3 ± 0.3	40.3 ± 1.9	1.8 ± 0.9	0.40 ± 0.02	7.96 ± 0.64
5	0.5	44.7 ± 0.3	42.2 ± 1.9	1.8 ± 0.9	0.41 ± 0.02	8.28 ± 0.65
Mean		**43.1 ± 3.8**	**41.8 ± 3.6**	**2.3 ± 1.4**	**0.40 ± 0.03**	**7.9 ± 1.1**

these techniques are mostly sensitive to the cross-planed atomic structure and electronic density of the layer stack. In the non-contact characterization landscape, the spectroscopic ellipsometry is also very interesting for its high thickness resolution, lower than the nanometer scale, even though it uses commonly optical wavelengths larger than the thickness of the stack under study. Such a performance is obtained because ellipsometry takes advantage of the polarization modification of the electric field vector by the materials, i.e. it collects both an amplitude and a phase information.

3.2.1. Dispersion model description

In our case, the model is composed only by a single layer over a semi-infinite layer of Nb:STO, as the LSMO film has been epitaxially grown onto a substrate with mirror-polished top surface. Backside specular reflections are avoided because of the rough non polished bottom surface of the substrate. The complex reflectivity r_{012} for such a single-layered heterostructure is given by the relation (14) in Appendix A.1, considering air as medium 0, LSMO thin film as medium 1 and Nb:STO substrate as medium 2.

The direct determination of the complex refractive index of the substrate $n_2 - jk_2$ is done before deposition, from its top surface specular reflection, thanks to relation (16) in Appendix A.1 taken from [13].

Obviously, the obtained substrate refractive index does not take into account correctly its absorption since it is based only on the analysis of the specular top surface reflected light. The $(n_2; k_2)$ extracted values constitute therefore "apparent" optical indexes. But their knowledge is necessary to extract in a reliable manner the complex refractive index of LSMO thin film deposited on it.

The LSMO is a strong correlated electron material with a metal-insulating (M-I) transition occuring at the temperature $T_{MI} \sim 360$ K, in parallel of a ferromagnetic - paramagnetic transition [26]. Although the LSMO is considered as a half-metal at room temperature, its electrical behaviour cannot be considered as a pure metallic one [31]. Logically, the chosen physical-based dispersion model has to take it into account, by mixing a Drude model $\epsilon_{r-Drude}$, suitable for metal, with an oscillator model for semiconductor ϵ_{r-SC}, derived from a modified Forouhi-Bloomer formulation.

By considering that the complex refractive index $\hat{n}_{LSMO}$ equals $\sqrt{\hat{\epsilon}_{r-Drude} + \hat{\epsilon}_{r-SC}}$, it is then easy to figure out the expressions for the optical index of refraction of LSMO n as well as its extinction coefficient k. A detail of this modeling is summarized in Appendix A.1. A complete mathematical description can also be found elsewhere, in technical notes of spectroscopic ellipsometry from the Horiba company, especially the Classical and New amorphous models.

3.2.2. Validation of the spectro-ellipsometric model

Only two oscillators are necessary in our case to describe correctly the experimental data, with a very good χ^2_{SE} value inferior to 1 for the five samples. This contrasts with Yamada *et al.* that have used seven Lorentz-type oscillators [9]. Such a difference in the oscillators number seems consistent with the reduced energy range explored in our study, compared to the data published by Yamada *et al.* that covers down to 0.03 eV in the very-long wave infrared range. In addition, instead of the classical modelling with only Lorentz oscillators, we have chosen a model including an optical energy gap to consider the insulating behaviour of LSMO, inherited from its parent oxide Mott insulator $LaMnO_3$ [32]. Figure 4 demonstrates clearly the good agreement of our proposed analytical model with the mean measured ellipsometric angles. One advantage of the ellipsometric study lies in the simultaneous determination of the complex optical index as well as of the thickness of each layer. First, we have made the assumption that the LSMO behaves like an isotropic medium, as Yamada *et al.* did [9]. Given its pseudo-cubic structure [25], we can reasonably think that such such LSMO layer does not require the use of Mueller matrix ellipsometry. In our case, the biaxial in-plane isotropy has been checked by the measurement of the sample in both perpendicular in-plane directions, in the same area, that does not reveal any difference in the $(\Psi_2; \Delta_2)$ spectra.

Table 4 summarizes some relevant parameters for the five

Table 4
Pseudo Forouhi–Bloomer and Drude model parameters for $La_{2/3}Sr_{1/3}MnO_3$ by spectro-ellipsometry (SE) analysis: chi-square fitting indicator χ^2_{SE}, high energy asymptotic refractive index n_∞, plasma oscillation ω_p, free carrier collision frequency Γ_d, optical gap ω_g and layer thickness h_{LSMO}. Values are given with a 2-σ uncertainty, including the sample dispersion for the mean values.

N°	χ^2_{SE}	n_∞	ω_p (eV)	Γ_d (eV)	ω_g (eV)	h_{LSMO} (nm)
1	0.81	1.67 ± 0.04	4.61 ± 0.09	2.42 ± 0.16	0.50 ± 0.57	39.2 ± 2.8
2	0.68	1.74 ± 0.03	4.67 ± 0.06	2.40 ± 0.13	1.18 ± 0.40	42.6 ± 2.7
3	0.69	1.76 ± 0.03	4.65 ± 0.06	2.44 ± 0.13	1.34 ± 0.28	40.9 ± 2.3
4	0.63	1.77 ± 0.03	4.70 ± 0.06	2.40 ± 0.13	1.10 ± 0.33	40.4 ± 2.4
5	0.71	1.78 ± 0.03	4.75 ± 0.06	2.49 ± 0.14	1.44 ± 0.32	42.5 ± 2.8
Mean		**1.74 ± 0.09**	**4.68 ± 0.12**	**2.43 ± 0.16**	**1.11 ± 0.83**	**41.1 ± 3.9**

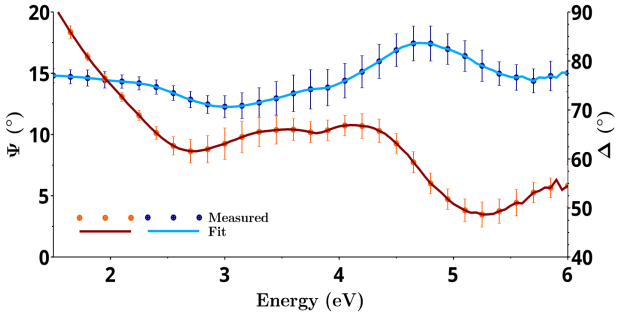

Figure 4: Ψ angle (blue line and marks) and Δ angle (orange line and marks) versus the incident photon energy. Comparison between the mean of the measured values over the five samples (marks) and the mean values computed by the fitting procedure (solid line). For clarity, only one third of experimental data points are represented with their 2-σ error bars.

measured samples. The LSMO layer quality between samples is demonstrated with relatively fair discrepancies between them. Nevertheless, we can draw two obvious observations by looking at those parameter values.

The first one is the low confidence on the mean extracted value for the optical energy gap ω_g, with a two third dispersion. One explanation could lie in the very smooth absorption peaks of the semiconducting part at ambient temperature, where the LSMO is dominated by a pseudo-metallic behaviour, like a degenerate semiconductor. However, the mean value of 1.1 eV is coherent with the gap of the insulating parent oxide, i.e. $LaMnO_3$ based on previous studies [33].

The second one is dealing with the thickness. The found values are in agreement with a mean relative error of 4.7 % with XRR result and 4.0 % with XRD result of Table 1. Moreover, the thickness uncertainty could be interpreted in terms of roughness, because its mean value of 2.6 nm is also consistent with the XRR analysis and the TEM cross-section observations.

Figure 5 illustrates clearly the fair uniformity of the LSMO layer properties between samples, with a mean experimental 2-σ deviation around 2.9 % both on the refractive index n and on the extinction coefficient k, averaged on the whole ellipsometry spectral range. As expected, the Nb doping, which stands under 1 % at, does not affect significantly the LSMO growth.

The two Drude parameters are within the same order of magnitude of already published values on $La_{2/3}Sr_{1/3}MnO_3$ films, i.e. around 10^{15} Hz for the collision frequency Γ_d and around 10^{15} rad.s^{-1} for the plasma frequency ω_p [30]. This study was based on Modulated Optical Reflectance (MOR) measurement at 633 nm, i.e. inside the wavelength range of our ellipsometric study. This qualitative agreement confirms the relevance of the Drude part in our dispersion model for such layer.

This knowledge of the complex refractive index can be used to simulate the reflectance of a single LSMO/Nb:STO heterostructure, using (14) or a matrix method whose formalism is well described in [11]. We are assuming an unpolarized light, i.e. the reflectance of the 012 layer stack R_{stack} can be expressed by:

$$R_{stack} = \frac{1}{2}\left(|r_{s-012}|^2 + |r_{p-012}|^2\right) \quad (8)$$

Figure 6 (b) shows the comparison between this calculation with the mean reflectance of samples n°1 to 4, measured by the spectrophotometer up to 5 eV, for an incidence angle of 8°. The experimental points from spectrophotometry are not equally spaced in energy because the instrument is sweeping linearly the wavelength λ unlike the energy sweeping of the spectro-ellipsometer.

There is a fair agreement between the two curves, especially in the 2.5 - 5 eV range, taking into account the sample dispersion. However, there is a discrepancy up to 2.8 % of absolute error in the 1.5 - 2.5 eV range, even more so because the dispersion is clearly reduced in this energy range, both for spectrophotometric and ellipsometric data.

Looking at the reflectance of the substrate only, in Figure 6 (a), we get a very good matching between both data, especially below 3 eV. The slight deviation is in this case more situated in the UV range, above 4 eV. The discrepancy observed for the specular reflectance of the heterostructure under 2.5 eV cannot thus be justified by the substrate itself

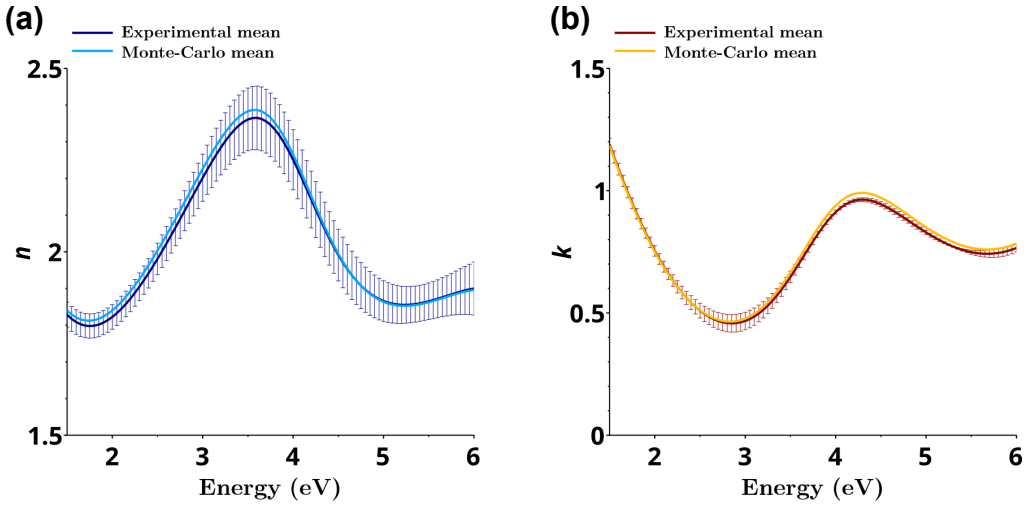

Figure 5: (a) The refractive index of the LSMO layer n as a function of energy. (b) The extinction coefficient of the LSMO layer k as a function of energy. Results are coming from spectroscopic ellipsometry measurement and data analysis, uncertainty error bars are represented only for experimental means. (a) and (b) Comparison of the experimental mean value between samples with the mean value computed by a Monte-Carlo method, with 10 000 random sampling, applied simultaneously on each gaussian-distributed LSMO dispersion model parameter, using 2-σ uncertainties given by the DeltaPsi2 software.

or any instrumental reason.

A plausible explanation is that it comes from the heteroepitaxial layer itself. As a matter of fact, the LSMO thin epilayer is fully strained, with an uniform biaxial in-plane tension and a proportional vertical compression, due to the intrinsic lattice mismatch with the Nb:STO substrate, as already described in the X-ray analysis section. Our single crystal epifilm LSMO (100) is thus in a tetragonal shape. This crystal system presents an uniaxial anisotropy in constrast to the isotropy of the theoretical perovskite cubic system. In that situation, the z component of the complex permittivity tensor, i.e. the complex refractive index $\hat{n}_z$, can differ from its in-plane components. With an incidence angle of 70°, the ellipsometry measurement was more sensitive to this difference than the spectrophotometry performed with a quasi-normal incidence angle of 8°. In other words, the apparent complex refractive index seen by ellipsometry is different from the one seen by reflectometry, which corresponds to the in-plane refractive index. Nevertheless, in the ratio $\rho(E)$ measured by ellipsometry, the only quantity affected by this effect is r_{p-012}, i.e. the electric field component parallel to the z axis. This maybe could justify the relative restrained difference between the two reflectance curves of Figure 6 (b).

The interpretation presented hereabove relies on the birefringent behaviour of our heteroepitaxial LSMO, with an extraordinary axis in the z direction, which is not the easiest optical axis to sense due to the nanometric film thickness.

3.2.3. Mass density determination of the LSMO layer

From the complex refractive index of LSMO, extracted by spectro-ellipsometry, it is then possible to estimate some other interesting properties, like the mass density of the LSMO layer. It can be calculated through the Clausius-Mossotti or Lorentz-Lorenz formula, knowing the refractive index n of the LSMO layer [34].

$$\frac{n^2-1}{n^2+2} = \frac{4}{3}\pi\alpha_m\rho_m\frac{N_A}{M} \tag{9}$$

where N_A is the Avogadro constant, M is the molecular weight of $La_{2/3}Sr_{1/3}MnO_3$ equals to 224.72 g.mol^{-1}, ρ_m is the mass density and α_m constitutes the molecular electronic polarizability of the LSMO. This latter quantity is equal to the sum of polarizability of each ion a_{ion} weighted by its stoechiometric factors inside the crystal. Theoretical polarizability values have been taken from literature [35]: $a_{La^{3+}} = 3.75\times10^{-24}$ cm^3, $a_{Sr^{2+}} = 2.01\times10^{-24}$ cm^3, $a_{Mn^{3+}} = 0.35\times10^{-24}$ cm^3, $a_{O^{2-}} = 0.75\times10^{-24}$ cm^3.

The calculation of the mass density with (9) is summarized in Table 5. The mean calculated value of 7.75 g.cm^{-3} reveals an experimental LSMO layer more dense than the theoretical value for the pseudo-cubic bulk LSMO of 6.345 g.cm^{-3} [36]. Nevertheless, the value found by ellipsometry analysis is rather consistent with the one from XRR analysis, with a relative error on the mean values of 1.4 %. This last result is another cross-validation of the spectro-ellipsometric measurement and modelling done on the LSMO layer. Physically, this apparent increasing could be related to the fully strained LSMO lattice, where appears in compression in z direction.

3.2.4. Drude model pertinence for LSMO

The $La_{2/3}Sr_{1/3}MnO_3$ presents a half-metallicity at room temperature [31], with a large number of free carriers directly related to its stoechiometry, i.e. coming from the Sr^{2+} deficient valence compared to La^{3+}, which induces a hole

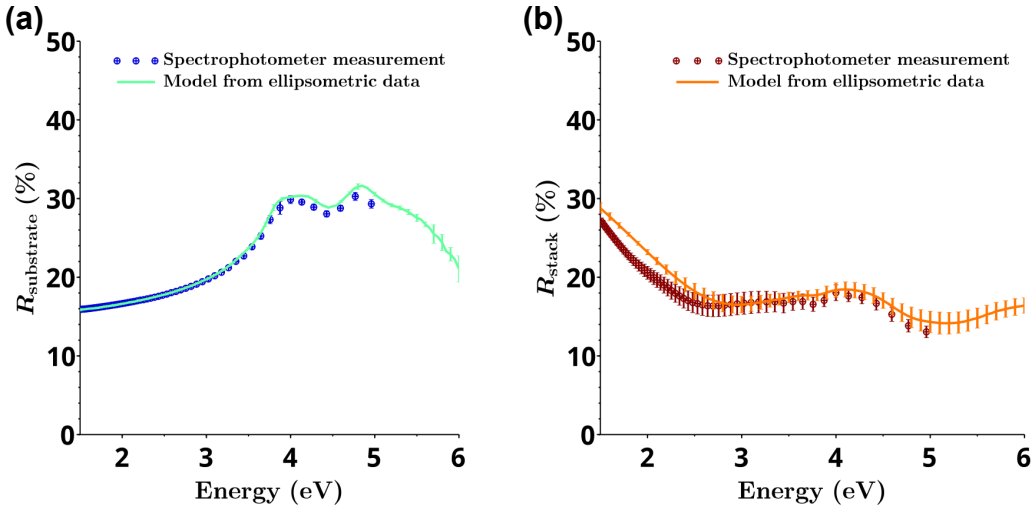

Figure 6: (a) Reflectance of the mirror top surface of an Nb:STO substrate, as a function of energy for an unpolarized light. This reflectance is similar for subtrates with doping concentration up to 0.1 %wt. The 0.5 %wt doped substrate is not included here because its reflectance spectrum in the studied energy range is lightly different, especially for energy inferior to 2 eV. (b) Reflectance of the studied LSMO/Nb:STO single heterostructure stack as a function of energy for an unpolarized light. (a) and (b) Comparison of the mean value of samples, measured by spectrophotometry, with the mean value calculated with ellipsometric data, notably the optical indexes of the LSMO layer and of the Nb:STO substrate. The error bars represent the 2-σ dispersion between samples.

Table 5
Mass density ρ_m and room temperature electrical resistivity ρ_{dc} of heteroepitaxial LSMO. Mean values are expressed including the 2-σ sample dispersion.

N°	[Nb] (%wt)	ρ_m (g.cm^{-3})	ρ_{dc} (mΩ.cm)
1	0	7.50 ± 1.79	1.57
2	0.01	7.71 ± 1.87	1.39
3	0.05	7.85 ± 1.85	1.47
4	0.1	7.82 ± 1.87	1.49
5	0.5	7.84 ± 1.86	-
Mean		**7.75 ± 1.87**	**1.48 ± 0.15**

doping [37]. The theoretical doping concentration N_f could be calculated thanks to the following formula.

$$N_f = \frac{N_A}{M}\rho_m x \tag{10}$$

where x is the molar fraction of Sr atoms inside the layer, i.e. $\frac{1}{15}$ with our stoechiometry. Taking $\rho_m = 7.75$ g.cm^{-3}, this leads to a N_{f-th} value about 1.4×10^{21} cm^{-3}.
It is also possible to extract an experimental value, combining ellipsometric data and values of the electrical resistivity ρ_{dc} at room temperature, i.e. 298 K, extracted from four-point probe measurement, using for example:

$$N_{f-exp} = \frac{m^*\Gamma_d}{q^2\rho_{dc}} \tag{11}$$

where q represents the elementary charge and m^* the effective carrier mass, taken equal as $3m_e$ for LSMO [30].
The mean extracted value of 4.2×10^{21} cm^{-3} is consistent with N_{f-th}, i.e. seems consistent. Here, the sample 5 has not been part of the calculation because the electrical conductivity of Nb:STO doped at 0.5 %wt at room temperature is higher than the one of LSMO, preventing its estimation from 4-point probe measurement.
Based on the Drude model definition, we can establish the following relation, theoretically valid for LSMO [9].

$$\Gamma_d = \epsilon_0\rho_{dc}\omega_p^2 \tag{12}$$

In this case, this leads to a mean value of 4.32 eV, i.e. quite the double compared to the 2.43 ± 0.16 eV of Table 4. However, this higher value is closer to the 4.59 eV previously deduced from MOR measurement [30].
This implies that the Drude parameters given by the ellipsometry analysis, i.e. the plasma frequency and the collision frequency, seems to be not self-consistent. This leads to an inconsistency between the extracted value of the free carrier concentration and the hole mobility value, taking into account the electrical resistivity measurement. A logical explanation is that the electrical Drude model by itself is not sufficient or suitable to calculate the true resistivity of the LSMO layer at room temperature, as suggested by the combined metal-insulator ellipsometric model used.

4. Conclusion

To conclude, the ability of the spectro-ellipsometry to give useful quantitative informations about complex oxide

heteroepitaxial structures, such as $La_{2/3}Sr_{1/3}MnO_3$ grown by PLD onto Nb doped $SrTiO_3$ substrates, was clearly demonstrated.

The spectro-ellipsometry analysis was here able to determine in parallel the thickness as well as other properties of a complex oxide epilayer, even using a refined complex permittivity dispersion model of ten parameters. This proof has been done by combining X-ray and optical measurements to improve the confidence and cross validate the results, within less than 5 % relative error between the different techniques. This type of careful comparison is scarsely present in the literature.

Moreover, the spectro-ellipsometry turned out to be the best tool to extract a full picture of the studied LSMO layer, namely the thickness h, the optical gap ω_g, the plasma frequency ω_p, the mass density ρ_m, the complex refractive index n and the extinction coefficient k between 1.5 to 6 eV photon energy range. This optical analysis has confirmed the need of a mixed dispersion model to report correctly the nature of the LSMO material and its measured electrical Metal-Insulator transition near the room temperature [26]. The proposed model, validated in this study, is a combination between a Drude model, adapted for metals, and a double-oscillator pseudo Forouhi-Bloomer model, adapted for insulating materials.

Finally, as a perspective, it could be interesting to check if the spectro-ellipsometry is really sensitive to the out-of-plane anisotropy of the LSMO layer. Further work would consist in using variable-angle optical measurements, both spectro-ellipsometry and spectrophotometry, always to cross validate the results by two different measuring techniques. The purpose of such study would be to differenciate quantitatively the out-of-plane uniaxial anisotropy of the fully strained LSMO heteroepitaxial layer, i.e. its birefringence, and to correlate it quantitatively with the strain found by X-ray diffraction.

CRediT authorship contribution statement

Jérémy Blond: Conceptualization, Methodology, Formal analysis, Visualization, Writing - original draft. **Christian Dufour:** Methodology, Formal analysis, Data curation, Writing-review editing. **Sandeep Kumar Chaluvadi:** Resources and Investigation. **Sylvain Duprey:** Investigation. **Xavier Portier:** Resources, Investigation. **Philippe Marie:** Resources, Investigation. **Victor Pierron:** Investigation. **Laurence Méchin:** Resources, Investigation, Data curation. **Bruno Guillet:** Supervision, Funding acquisition, Methodology, Data curation, Writing-review editing.

Acknowledgements

J. Blond would like to thank the University of Caen Normandie for the postdoctoral fellowship. X. Portier is grateful to the ANR (Agence Nationale de la Recherche) and the Normandy Region for their financial support in acquiring the FIB system, and thanks F. Lemarié for the TEM foils preparation. The TEM investigation falls within the scope of the research foundation IRMA (FR 3095).

A. Appendix

A.1. Spectro-ellipsometry relations

The complex reflectance ratio ρ is defined by:

$$\rho = \tan(\Psi)\, e^{j\Delta} = \frac{r_p}{r_s} \tag{13}$$

Where r_p and r_s are the complex electric field reflectivities for the parallel and perpendicular direction from the incidence plan espectively. The complex reflectivity r_{012} for a single-layered heterostructure with air as medium 0, thin film as medium 1 and substrate as medium 2 is given by:

$$r_{012} = \frac{r_{01} + r_{12} e^{-2j\hat{\beta}_1}}{1 + r_{01} r_{12} e^{-2j\hat{\beta}_1}} \tag{14}$$

The previous relation is valid whatever the considered incidence angle θ_0 and for each polarization of the light regarding the incidence plane, i.e. parallel (p-polarized) or perpendicular (s-polarized). $\hat{\beta}_1$ designates the phase angle inside medium 1 given by:

$$\hat{\beta}_1 = \frac{2\pi}{\lambda} h_1 \hat{n_1} \cos\left(\arcsin\left(\sin\left(\frac{\theta_0}{\hat{n_1}}\right)\right)\right) \tag{15}$$

It exists an unambiguous relation between complex refractive index of the substrate $n_2 - jk_2$ and the couple $(\Psi_2; \Delta_2)$ measured by the ellipsometer, given by the expression with air as prime medium.

$$n_2 - jk_2 = \sin\theta_0 \left[1 + \left(\frac{1-\rho_2}{1+\rho_2}\right)^2 \tan^2\theta_0\right]^{\frac{1}{2}} \tag{16}$$

In the hereafter equations, the Horiba expressions are using the pulsation ω to illustrate the spectral dependence of the LSMO, which is equivalent to the photon energy E divided by the coefficient $\hbar$.

$$\hat{n}^2_{LSMO} = \hat{\epsilon}_{r-LSMO} = \hat{\epsilon}_{r-Drude} + \hat{\epsilon}_{r-SC} \tag{17}$$

$$\Leftrightarrow \hat{n}_{LSMO} = n - jk = \left[-\frac{\omega_p^2}{\omega^2 + j\Gamma_d\omega} + \hat{n}^2_{SC}\right]^{\frac{1}{2}}$$

$$\text{where} \begin{cases} \omega_p : \text{plasma oscillation frequency} \\ \Gamma_d : \text{free carrier collision frequency} \end{cases}$$

$$n_{SC} = n_\infty + \sum_{m=1}^{2} \frac{B_m(\omega - \omega_m) + C_m}{(\omega - \omega_m)^2 + \Gamma_m^2} \tag{18}$$

$$\text{where} \begin{cases} B_m = \frac{f_m}{\Gamma_m}\left[\Gamma_m^2 - (\omega_m - \omega_g)^2\right] \\ C_m = 2 f_m \Gamma_m (\omega_m - \omega_g) \end{cases}$$

$$k_{SC} = \begin{cases} \sum_{m=1}^{2} \frac{f_m(\omega-\omega_g)^2}{\left[(\omega-\omega_m)^2 + \Gamma_m^2\right]} & \text{for } \omega > \omega_g \\ 0 \text{ either.} \end{cases} \tag{19}$$

where

$$\begin{cases} n_\infty : \text{limit of } n_{SC} \text{ where } \omega \to \infty \\ \omega_g : \text{optical gap} \\ \omega_m : \text{absorption peak angular frequency of the m}^{th} \text{ oscillator, with } \omega_m > \omega_g \\ f_m : \text{amplitude of the absorption peak of the m}^{th} \text{ oscillator} \\ \Gamma_m : \text{FWHM of the absorption peak of the m}^{th} \text{ oscillator} \end{cases}$$

A.2. Mass density from XRR

First, the electron density of the top single layer on a substrate is derived.

$$\rho_e = \frac{2\pi}{\lambda^2 r_e}\delta = \frac{\pi}{\lambda^2 r_e}\theta_c^2 \tag{20}$$

where r_e is the electron radius, taken equal to 2.813×10^{-5} Å. Then, the mass density can be estimated thanks to the following equation, neglecting the absorption.

$$\rho_m = \rho_e \left[N_A \sum_i x_i \frac{Z_i + f_i'}{M_i} \right]^{-1} \tag{21}$$

where N_A is the Avogadro constant, x_i is the molar fraction of atom i, Z_i is the atomic number of atom i, M_i is the molar mass of atom i and f_i' is the real part of the anomalous scattering factor for the used X-ray reflectivity wavelength [38].

Data collected and used for the $La_{2/3}Sr_{1/3}MnO_3$ is summarized in Table 6.

Table 6
Data for LSMO mass density estimation from XRR measurement

Atom i	x_i (%)	M_i (g.mol^{-1})	Z_i	f_i'
La	0.13	138.91	57	-1.27
Sr	0.07	87.62	38	-0.33
Mn	0.20	54.94	25	-0.60
O	0.60	16.00	8	0.05

References

1. Postma, F. M. *et al.* Epitaxial diodes of a half-metallic ferromagnet on an oxide semiconductor. *J. Appl. Phys.* **95,** 7324–7326. http://aip.scitation.org/doi/10.1063/1.1669255 (June 2004).
2. Ruotolo, A., Lam, C. Y., Cheng, W. F., Wong, K. H. & Leung, C. W. High-quality all-oxide Schottky junctions fabricated on heavily Nb-doped $SrTiO_3$ substrates. *Phys. Rev. B* **76,** 075122 (2007).
3. Hu, F., Gao, J., Sun, J. & Shen, B. Good rectifying characteristic in p–n junctions composed of La 0.67 Ca 0.33 MnO 3- δ/Nb–0.7 wt%-doped SrTiO 3. *Appl. Phys. Lett.* **83,** 1869–1871 (2003).
4. Kurij, G. *et al.* Ultrathin junctions based on the $LaSrMnO_3$/Nb:$SrTiO_3$ functional oxide interface. *Thin Solid Films* **617,** 82–85. https://linkinghub.elsevier.com/retrieve/pii/S004060901630027X (Oct. 2016).
5. Zhi-Hui, S., Ting-Yin, N., Yue-Liang, Z., Song-Qing, Z. & Ling-Zhu, C. Photovoltaic Characteristic of $La_{0.7}Sr_{0.3}MnO_3$/ZnO p-n Heterojunction. *Chin. Phys. Lett.* **25,** 1861. https://iopscience.iop.org/article/10.1088/0256-307X/25/5/092/meta (May 1, 2008).
6. Liu, H.-J. *et al.* Giant Photoresponse in Quantized $SrRuO_3$ Monolayer at Oxide Interfaces. *ACS Photonics* **5,** 1041–1049. https://doi.org/10.1021/acsphotonics.7b01339 (Mar. 21, 2018).
7. Muramatsu, T., Muraoka, Y. & Hiroi, Z. Photocarrier injection and the I–V characteristics of $La_{0.8}Sr_{0.2}MnO_3$/$SrTiO_3$:Nb heterojunctions. *Solid State Commun.* https://www.scinapse.io (Nov. 1, 2004).
8. Sheng, Z. G. *et al.* Magneto-tunable photocurrent in manganite-based heterojunctions. *Nat Commun* **5,** 4584. http://www.nature.com/articles/ncomms5584 (Dec. 2014).
9. Yamada, Y., So, J., Asano, H., Tazawa, M. & Yoshimura, K. Temperature dependence of optical constants of $La_{0.7}Sr_{0.3}MnO_3$ thin films. *Appl. Surf. Sci. 7th_International Conference on Spectroscopic Ellipsometry* **421,** 866–869. https://www.sciencedirect.com/science/article/pii/S0169433217304129 (Nov. 1, 2017).
10. Drévillon, B. Phase modulated ellipsometry from the ultraviolet to the infrared: in situ application to the growth of semiconductors. *Prog. Cryst. Growth Charact. Mater.* **27,** 1–87 (1993).
11. Hébert, M., Simonot, L. & Mazauric, S. Matrix method to predict the spectral reflectance of stratified surfaces including thick layers and thin films. *HAL open archive - preprint* (2015).
12. Drant, T. *et al.* Optical constants of exoplanet haze analogs from 0.3 to 30 µm: Comparative sensitivity between spectrophotometry and ellipsometry. *A&A* **682,** A6. https://www.aanda.org/10.1051/0004-6361/202346820 (Feb. 2024).
13. HORIBA. Spectroscopic Ellipsometry User Guide (2008).
14. HORIBA. *DeltaPsi2: Fully Integrated Spectroscopic Ellipsometry Software Package* https://static.horiba.com/fileadmin/Horiba/Products/Scientific/Emerging_Businesses/DeltaPsi2/TN-03_-_DeltaPsi2-LR.pdf (2024).
15. Glavic, A. & Björck, M. *GenX 3* : the latest generation of an established tool. *J Appl Crystallogr* **55,** 1063–1071. https://scripts.iucr.org/cgi-bin/paper?S1600576722006653 (2023) (Aug. 1, 2022).
16. Smits, F. M. Measurement of Sheet Resistivities with the Four-Point Probe. *Bell Syst. Tech. J.* **37,** 711–718 (1958).
17. Perloff, D. S. Four-point sheet resistance correction factors for thin rectangular samples. *Solid State Electron.* **20,** 681–687. https://linkinghub.elsevier.com/retrieve/pii/0038110177900442 (Aug. 1977).
18. Pietsch, U., Holý, V. & Baumbach, T. *High-Resolution X-Ray Scattering* ISBN: 978-1-4419-2307-3 978-1-4757-4050-9. http://link.springer.com/10.1007/978-1-4757-4050-9 (Springer, New York, NY, 2004).
19. Ying, A. J., Murray, C. E. & Noyan, I. C. A rigorous comparison of X-ray diffraction thickness measurement techniques using silicon-on-insulator thin films. *J Appl Crystallogr* **42,** 401–410. https://journals.iucr.org/paper?ks5206 (2009).
20. Lichtensteiger, C. *InteractiveXRDFit* : a new tool to simulate and fit X-ray diffractograms of oxide thin films and heterostructures. *J Appl Crystallogr* **51,** 1745–1751. https://scripts.iucr.org/cgi-bin/paper?S1600576718012840 (Dec. 1, 2018).
21. Durand, O., Letoublon, A., Rogers, D. & Hosseini Teherani, F. Interpretation of the two-components observed in high resolution X-ray diffraction scan peaks for mosaic ZnO thin films grown on c-sapphire substrates using pulsed laser deposition. *Thin Solid Films* **519,** 6369–6373. https://linkinghub.elsevier.com/retrieve/pii/S0040609011008522 (July 2011).
22. Ryang Wie, C. High resolution x-ray diffraction characterization of semiconductor structures. *Mater. Sci. Eng., R* **13,** 1–56. https://linkinghub.elsevier.com/retrieve/pii/0927796X94900086 (Sept. 15, 1994).

23. in. *High-Resolution X-Ray Scattering from Thin Films and Multilayers* (eds Holý, V., Pietsch, U. & Baumbach, T.) 119–149 (Springer, Berlin, Heidelberg, 1999). ISBN: 978-3-540-49625-0. https://doi.org/10.1007/BFb0109392.

24. Lyonnet, R., Maurice, J.-L., Hÿtch, M., Michel, D. & Contour, J.-P. Heterostructures of $La_{0.67}Sr_{0.33}MnO_3/SrTiO_3/La_{0.67}Sr_{0.33}MnO_3$ grown by pulsed laser deposition on (001) $SrTiO_3$. *Appl. Surf. Sci.* **162,** 245–249 (2000).

25. Haghiri-Gosnet, A.-M. & Renard, J.-P. Topical review: CMR manganites: physics, thin films and devices. *J. Phys. D: Appl. Phys.* **36,** R127 (2003).

26. Méchin, L. *et al.* Experimental evidence of correlation between 1/ *f* noise level and metal-to-insulator transition temperature in epitaxial $La_{0.7}$ $Sr_{0.3}$ MnO_3 thin films. *J. Phys. D: Appl. Phys.* **46,** 202001. https://iopscience.iop.org/article/10.1088/0022-3727/46/20/202001 (May 22, 2013).

27. Gibaud, A., Chebil, M. S. & Beuvier, T. in *Surface Science Techniques* (eds Bracco, G. & Holst, B.) Series Title: Springer Series in Surface Sciences, 191–216 (Springer Berlin Heidelberg, Berlin, Heidelberg, 2013). ISBN: 978-3-642-34242-4 978-3-642-34243-1. https://link.springer.com/10.1007/978-3-642-34243-1_7.

28. Durand, O. & Morizet, N. Fourier-inversion and wavelet-transform methods applied to X-ray reflectometry and HRXRD profiles from complex thin-layered heterostructures. *Applied Surface Science* **253,** 133–137. https://linkinghub.elsevier.com/retrieve/pii/S0169433206008282 (Oct. 2006).

29. Bridou, F. *et al.* Thin multilayers characterization by grazing X-ray reflectometry and use of Fourier transform. *Appl. Surf. Sci.* **253,** 12–16. https://linkinghub.elsevier.com/retrieve/pii/S0169433206007781 (Oct. 2006).

30. Méchin, L., Flament, S., Perry, A., Almond, D. P. & Chakalov, R. A. Modulated optical reflectance measurements on $La_{2/3}Sr_{1/3}MnO_3$ thin films. *J. Appl. Phys.* **98,** 103902. http://aip.scitation.org/doi/10.1063/1.2128693 (Nov. 15, 2005).

31. Graziosi, P. *et al.* Polaron framework to account for transport properties in metallic epitaxial manganite films. *Phys. Rev. B* **89,** 214411. https://link.aps.org/doi/10.1103/PhysRevB.89.214411 (June 12, 2014).

32. Arima, T., Tokura, Y. & Torrance, J. B. Variation of optical gaps in perovskite-type 3d transition-metal oxides. *Phys. Rev. B* **48,** 17006–17009. https://link.aps.org/doi/10.1103/PhysRevB.48.17006 (Dec. 15, 1993).

33. Kitamura, M. *et al.* Determination of band diagram for a *p-n* junction between Mott insulator $LaMnO_3$ and band insulator Nb:$SrTiO_3$. *Appl. Phys. Lett.* **106,** 061605. https://pubs.aip.org/apl/article/106/6/061605/29222/Determination-of-band-diagram-for-a-p-n-junction (Feb. 9, 2015).

34. Horcholle, B. *et al.* Growth and study of Tb3+ doped Nb_2O_5 thin films by radiofrequency magnetron sputtering: Photoluminescence properties. *Appl. Surf. Sci.* **597,** 153711. https://linkinghub.elsevier.com/retrieve/pii/S0169433222012600 (Sept. 2022).

35. Ghosh, D. C. & Biswas, R. Theoretical Calculation of Absolute Radii of Atoms and Ions. Part 2. The Ionic Radii. *Int. J. Mol. Sci.* **4.** Number: 6 Publisher: Molecular Diversity Preservation International, 379–407. https://www.mdpi.com/1422-0067/4/6/379 (June 2003).

36. Gellé, F. *Hétérostructures épitaxiées avec des propriétés dépendantes de spin et de charges pour des applications en spintronique* These de doctorat (Strasbourg, Nov. 27, 2019). https://www.theses.fr/2019STRAE032.

37. *Thin Film Metal-Oxides* (ed Ramanathan, S.) (Springer US, Boston, MA, 2010). ISBN: 978-1-4419-0663-2 978-1-4419-0664-9. http://link.springer.com/10.1007/978-1-4419-0664-9.

38. Merritt, E. A. *Anomalous X-ray Scattering Coefficients* Accessed on 02.14, 2024. 2011. http://skuld.bmsc.washington.edu/scatter/AS_form.html.